Optimum telescope focal ratios for microlens-to-fiber coupled integral field spectrographs

Sabyasachi Chattopadhyay[©], ^{a,*} Matthew A. Bershady, ^{a,b,c} Marsha J. Wolf, ^b and Michael P. Smith^b

^aSouth African Astronomical Observatory, Observatory, Cape Town, South Africa ^bUniversity of Wisconsin, Department of Astronomy, Madison, Wisconsin, United States ^cUniversity of Cape Town, Department of Astronomy, Rondebosch, South Africa

Abstract. We describe the optimum telescope focal ratio for a two-element, three-surface, telecentric image-transfer microlens-to-fiber coupled integral field unit within the constraints imposed by microoptics fabrication and optical aberrations. We create a generalized analytical description of the microoptics optical parameters from first principles. We find that the optical performance, including all aberrations, of a design constrained by an analytic model considering only spherical aberration and diffraction matches within $\pm 4\%$ of a design optimized by raytracing software such as Zemax. The analytical model does not require any compromise on the available clear aperture; about 90% mechanical aperture of hexagonal microlens is available for light collection. The optimum telescope f-ratio for a 200- μ m core fiber-fed at f/3.5 is between f/7 and f/12. We find the optimum telescope focal ratio changes as a function of fiber core diameter and fiber input beam speed. A telescope focal ratio of f/8 would support the largest range of fiber diameters (100 to 500 μ m) and fiber injection speeds (between f/3 and f/5). The optimization of the telescope and lenslet-coupled fibers is relevant for the design of high-efficiency dedicated survey telescopes, and for retrofitting existing facilities via introducing focal macro-optics to match the instrument input requirements. © 2022 Society of Photo-Optical Instrumentation Engineers (SPIE) [DOI: 10.1117/1.JATIS.8.2.025001]

Keywords: integral field spectroscopy; microlens-fiber IFU; microlens optical design: telescope f-ratio.

Paper 21163G received Dec. 13, 2021; accepted for publication Apr. 14, 2022; published online May 5, 2022.

1 Introduction

Modern-day spectroscopic surveys employ collecting apertures running from 10-m class telescopes (VIRUS),^{1,2} prime focus spectrograph (PFS),³ and Maunakea spectroscopi explorer (MSE)⁴), to modest 4-m class telescopes [e.g., dark energy spectroscopic instrument (DESI)⁵ and 4MOST⁶], down to even a few hundred mm (local volume mapper⁷). At the heart of each of these surveys is fiber-optic coupled spectroscopy. Fiber optics serve as a convenient bridge between the mobile telescope system and the more stable spectrograph mounts, as well as a image reformatting system from the telescope focal plane to spectrograph entrance slit. While galactic and extragalactic surveys have traditionally employed single fibers to multiplex redshift and spectral diagnostic measurements of stars, distant galaxies and quasars, more recently there has been an additional focus on mapping resolved sources (nearby galaxies and galactic nebulae) using integral-field spectroscopy (IFS). In general, fiber-fed IFS [integral field unit (IFUs); e.g., SparsePak, PPak, VIRUS-P, VIRUS-W, MaNGA, and MEGARA 11 are flexible, costeffective, and suitable for optical and near-IR wavelengths. Fibers also lend themselves well to multiobject IFS of distributed and/or extended sources contained in large (often many deg²) telescope fields of view (e.g., SAMI¹² on the 4 m AAT and MaNGA¹³ on the 2.5 m Sloan Telescope). Consequently, fiber-fed IFS remains an appealing approach alongside other flavors of IFS (e.g., image-slicing with SPHERE, 14 multi-unit spectroscopic explorer, 15 and K-band multi-object spectrometer¹⁶ on very large telescope, or keck cosmic web imager¹⁷ on Keck).

2329-4124/2022/\$28.00 © 2022 SPIE

J. Astron. Telesc. Instrum. Syst.

025001-1

^{*}Address all correspondence to Sabysachi Chattopadhyay, sabyasachi@saao.ac.za

Despite fiber optics being a popular and cost-effective mode of coupling telescopes to spectrographs, fibers are well-known to degrade the input focal ratio upon output. This focal ratio degradation (FRD) via stepped index, multimode fibers^{18–20} affects the efficiency of observation because it is, in essence, an injection of entropy into the information gathering system. It is observed^{21,22} that the effect of FRD can be minimized by injecting a faster beam into the fiber.

A contemporary measurement of this effect is illustrated in Fig. 1 using a differential reimaging system similar to Refs. 8, 10, and 23. The FRD was measured for a 2-m length of $400-\mu m$ diameter core step-index, broad-band fiber (MOLEX/Polymicro FBP400:440:470) fed with a centered, reimaged near-field spot of $100~\mu m$ in diameter. The input focal ratio was varied by changing the aperture of an intermediate pupil-stop. The output focal ratio was measured at a radius covering 98% of the normalized encircled energy (EE). The salient feature of this measurement was that it was performed with a well-aligned inject beam, telecentric to within 0.1 deg in tip/tilt similar to that of Ref. 23. The upper limit on the angular deviation limits geometric FRD (gFRD) to no faster than f/286; over the range of injection speeds, this is inconsequential. While the left-hand panel of Fig. 1 shows the well-known nonlinear "saturation" of the output beam speed, in the right panel we present the same measurements as a ratio of out versus input solid angle. This has a simple, linear behavior with input numerical aperture from which entropy gain due to fiber FRD can be easily estimated. The qualitative behavior motivates why present-day fiber-coupled spectrographs tend to have faster collimators (see the references above).

It is also the case that for IFS using bare, densely packed circular fibers, the fill factor is typically only 60% ¹⁰ given the inherent geometry plus the minimum requirements for cladding and mechanical buffer. Some gains can be had by removing the buffer and lightly fusing the fibers, but is technically challenging and comes at the cost of more FRD. ²⁴ Consequently, it is often desirable to couple fibers to the telescope focal plane via lenslet arrays. One purpose of lenslet coupling is to increase the fill factor of the fiber array. In principle, circular lenslets with hexagonal packing or hexagonal lenslets with circular chromium coating can increase the fill factor up to 90%. We consider this lenslet geometry in this paper. However, when coupling lenslets to fibers, a further challenge arises: The clear aperture in a microlens system falls quickly compared with the available mechanical aperture with faster input beams from telescope. ^{25,26} Thus in an effort to reduce FRD one would struggle to attain an acceptable fill factor on sky. ²⁵

The aim of this study is to resolve the tension between the optimum input focal ratios for lenslet and fiber optics. This is part of the broader question, i.e., given a survey being planned, either using an existing telescope or a new telescope, what would be the ideal telescope focal ratio at the input of the microlens for a set of fiber input speed, fiber diameter, and fabricable microlens properties. To do so we develop a generic analytical description of an image transfer IFU optical model to optimize the telescope focal ratio within the constraints posed by the

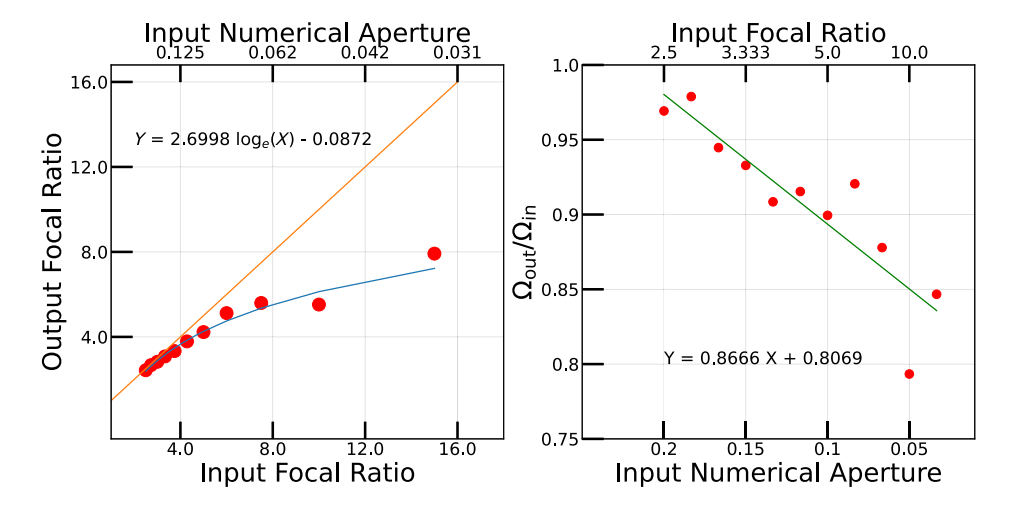


Fig. 1 FRD by a 2-m long 400-μm diameter core fiber for various input focal ratio measured at a normalized EE of 98%. Measurements details are described in the text. The figure depicts the effect of FRD via fiber increases with slower input beam in the left panel while the right panel shows the linear loss of solid angle on sky with decreasing input numerical aperture.

J. Astron. Telesc. Instrum. Syst.

025001-2

microlens array fabrication. We assume the spectrograph design accommodates a fast fiber output beam or, alternatively, uses additional microlenses at the output end of the fiber to modulate the speed of the spectrograph collimator. We start in Sec. 2 by describing the optical parameters of an image transfer IFU system and the parameter space available for optimization given fabrication limitations and FRD. In Sec. 3 we describe the analytical model to define the IFU optical parameters. The following sections discuss two distinct regimes where on-axis aberrations are either dominated by diffraction or spherical aberration (SA) (Sec. 4) and the design choices that minimize light loss from aberrations in general (Sec. 5). We confirm the reliability of our model compared with ray-trace calculations in the nondiffraction-limited regime in Sec. 5 as well. In Sec. 6, we describe the acceptable range of telescope beam speed defined by the fabrication limits. Section 7 summarizes our results and presents our conclusions.

The result of our analysis calls for much slower telescope beams than developed for telescopes optimized for bare-fiber feeds, such as HET and SALT, which are close to f/4. The optimum telescope f-ratio we find is closer to f/8, although in detail we will show this depends on the fiber core diameter. The optimum f-ratio can be achieved on an existing telescope via a macrofocal reducer or expander. However, for a dedicated survey facility, we suggest optimizing the native telescope beam speed to minimize the total number of optical elements. 30,31

2 Design Choices and Constraints

2.1 Image Transfer Microlens System

We describe telecentric reimaging (or image-relay) microlens systems in this paper, and note differences with pupil-transfer microlens systems below. The basic optical concept is to re-image the focal plane onto the fiber cores through a set of two MLAs. Conceptually, the first MLA elements act as field lenses while the second produces telecentric images. In practice, to optimize image quality the optics deviate slightly from this idealized prescription (see, e.g., VIRUS2 design and Sec. 5 here). A biconvex MLA (BC) with an appropriate radius of curvature (RoC) and thickness creates a pupil at its exit surface, and the exit beam is collimated for all field points. A suitable gap (depending on the RoC of the second MLA) between the BC and plano-convex MLA (PC) ensures a telecentric image at the flat back surface of the PC.

One of the free design parameter is the microimage size at the input of the fiber. However, in our previous study, 26 we found that the microimage diameter should be $\sim 97\%$ of the fiber core diameter to minimize étendue gain. Thus the fiber core diameter and microimage diameter are used interchangeably in our analysis. To maximize grasp (area–solid-angle product, or $A\Omega$), the ideal microimage diameter (d_m) should be equal to the diameter of the fiber core. However, fiber positioning and alignment issues d_m needs to be smaller than the fiber core. Based on our own photo-lithographic work and comparison to commercially available products we estimate current technology permits fibers to be positioned within ± 3 - μ m RMS at any desired spacing. 26

Figure 2 illustrates a typical image-relay microlens system where telescope light is fed at a focal ratio of f_{tel} . This beam enters the BC microlens with r_b radius of curvature, D_b thickness, and d_a clear aperture. The thickness is defined such that the beam forms its pupil at the exit

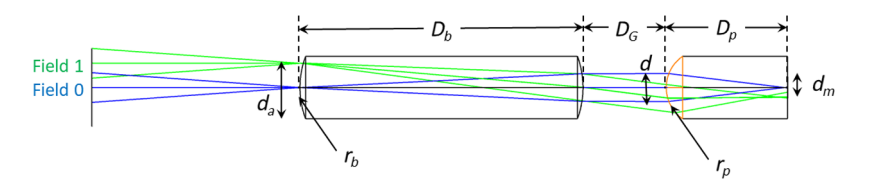


Fig. 2 Arrangement of a reimaging microlens array system that captures a part of the telescope focal plane (d_a) and injects this into the fiber core. Key design parameters are (a) field 0: central field point; (b) field 1: edge field point; (c) d_a : diameter of the input beam/BC microlens clear aperture diameter; (d) r_b : BC radius of curvature; (e) D_b : BC thickness; (f) d: field 0 pupil diameter; (g) r_p : PC microlens radius of curvature; (h) D_p : PC thickness; (i) D_G : air gap width between PC and BC; (j) d_m : microimage diameter/fiber core diameter. Details about implemented microlens properties are discussed in Ref. 32.

J. Astron. Telesc. Instrum. Syst.

025001-3

surface of the BC microlens. The pupil is then focused on an image plane via a PC lens with r_p radius of curvature and D_p thickness, sitting at a distance of D_G from the BC lens. D_p and the beam diameter of the central field defines the injected f-ratio ($f_{\rm fib}$) into the fiber. Since the pupil is positioned at the exit surface of the BC MLA, one can define D_p as $n_g \times r_p/(n_g-1)$ so that the PC microlens produce telecentric microimage at its planar back plane. Thus $f_{\rm fib}$ and hence d and D_p define r_p as well. On the other hand, D_G defines the MLA clear aperture diameter which in turn defines the sky sampling size (via plate scale). We provide mathematical prescriptions of all these dependencies in the following Sec. 3 and more details about their derivation can be found in Appendix A.

2.2 Other Microlens Systems

Other microlens relay options include transfer of the image with a pupil onto the fiber entrance aperture. These so-called pupil-transfer systems have the advantage of requiring only one MLA. In the simplest case using a single PC MLA can be bonded directly to the fiber to minimize reflection losses. Unfortunately, the pupil image onto the fiber is not telecentric, leading to potentially significant gFRD. Because the fibers azimuthally scramble the input signal, the nontelecentric feed cannot be corrected at the fiber output. It is straightforward to correct this by replacing the PC MLA with something similar to the biconvex MLA seen in Fig. 2. Consequently, pupil-transfer systems will have similar, but simpler descriptions and constraints compared with the image-relay microlens systems. For this reason, we break out the constraints from both the BC and PC elements.

2.3 Merit of Telecentric Designs

While the reimaging MLA system does not require additional air-glass surfaces to create a telecentric design, it does place constraints on the lenslet design as we will see below. Further, as noted above a telecentric pupil-imaging MLA system does require the addition of two air-glass surfaces. Broadly, it is worth considering whether imposing telecentric designs are worth the cost in either design constraints or reflection losses. It is easiest to understand this in the context of the pupil-imaging MLA system as follows.

As a general, qualitative statement for the telecentric pupil-imaging MLA case, given modern multilayer antireflection coatings with broad-band performance achievable at 0.5% to 1% reflection loss per air-glass surface over more than an octave in wavelength, the bar is not set very high to gain by adding a two air-glass surfaces to eliminate gFRD.

Equation 3 of Ref. 33 can be used to compute the throughput loss due to gFRD. The fraction of the light lost is given by $L \sim (0.4/B)(\delta/u)$ where u is the angle of the marginal ray with respect to the apex of the telecentric beam, δ is the angle of the marginal ray in the nontelecentric beam with respect to the apex of the telecentric beam at the field edge, and B is the fractional area of the telescope primary mirror unobscured by the secondary mirror. The angles in a PC MLA pupil-imaging system are illustrated in Fig. 3. As two representative extrema, B has a value of about 0.95 for the Gemini 8 m telescope³⁴ and a value of about 0.7 for the Sloan 2.5m telescope.³⁵

Figure 3 shows that gFRD already leads from 10% to 30% throughput loss for $f_{\rm tel}=10$ (depending on fiber injection speed and telescope central obstruction), and this increases rapidly for faster telescopes. For any plausible telescope f-ratio, uncorrected gFRD losses never fall below 1%. This makes it clear that the telecentric design is preferable in all relevant cases for pupil imaging. For reference, the GMOS IFU on Gemini³⁶ has a PC MLA lenslet system fed at f/50 and injecting light into the fibers at f/4. This system should have \sim 5% thoughtput loss due to gFRD.

2.4 Critical Design Parameter Space for Image-Relay Microlens Systems

The primary design parameters that have bearing on manufacturing limitations include the surface curvature given by r_p and r_b , and the MLA thickness D_b or D_p . Based on discussion with, e.g., $A\mu S$ (advanced microoptic systems³⁷), we specify these fabrication-based limits for these parameters:

J. Astron. Telesc. Instrum. Syst.

025001-4

Fig. 3 Ray schematic for the nontelecentric PC MLA pupil-imaging fiber system (left). The telescope focal plane is formed at the location of the left-most vertical dashed line. Blue rays trace the telescope pupil formed by the lenslet and also the fiber-input light cones at the edge of the fiber. The chief ray of these cones is at an angle δ with respect to the telecentric angle. Red rays (dashed) trace the input cone on the fiber face at the field center, with a marginal ray angle u. The geometric FRD loss based on Ref. 33 is shown at right for two telescope central obstructions of 5% (black) and 30% (red), and two fiber input beam speeds (f/3 and f/5 in air, bottom and top curves, respectively, for each color). The lenslet and fiber index of refraction is assumed to be matched at $n_g = 1.46$.

- 1. Maximum manufacturing limitation on the thickness (D_b or D_p) of a microlens of 10 mm and a minimum of 0.3/0.6 mm for PC and BC MLA, respectively.
- 2. Fabrication limitation on the minimum radius of curvature of a microlens $(r_b \text{ or } r_p)$ of 0.02 mm.

The specific values for these parameters depend on the fiber input f-ratio $f_{\rm fib}$ and microimage diameter d_m as well as $f_{\rm tel}$. We also bound $f_{\rm fib}$ and d_m in our analysis, as follows, leaving $f_{\rm tel}$ unbounded. We constrain d_m by the range of off-the-shelf multimode fiber size, with 50 μ m as the smallest, and 600 μ m as the largest that has seen practical use.³⁸

The range of $f_{\rm fib}$ depends on the range of acceptable f-ratios for the spectrograph input (the collimator). Traditional spectrograph designs have preferred slow collimators to increase spectral resolution by decreasing the angular size of the slit while keeping the overall beam size as small as possible. Slower input beams offer the added opportunity of demagnification via fast camera optics to optimize matching to detector focal-planes. However, with fiber coupling, FRD requires collimator speeds of f/5 to prevent significant loss of etendue, as seen in successful fiber-fed spectrograph designs (Hectoechelle, 39 GIRAFF, 40 upgraded WIYN Bench, 41 and SDSS/BOSS 42). Indeed, in more recent designs (e.g., DESI-f/3.7, 5 M2FS-f/3.4, 43 WEAVE-f/3.1, 44 MEGARA-f/3, 11 PFS-f/2.8, 3 and DOTIFS-f/4.5 45), collimators are substantially faster to further minimize FRD. Spectrograph collimators are able to accept f/2.5 with standard off the shelf optics while custom modification may able to grasp faster beams 46 approaching the fiber numerical aperture (typically f/2.2 for standard, high-transmission broad-bandpass step-index fiber). We take $2.5 < f_{\rm fib} < 5$ to be a reasonable range for this parameter to keep FRD-induced entropy increase minimal to modest (see Fig. 1) in standard step-index fiber optics with numerical apertures of 0.22, most commonly used in astronomical instrumentation.

In summary, then:

- 3. Fiber diameter d_m between 50 to 600 μ m.
- 4. Fiber input beam speed f_{fib} between f/2.5 and f/5.

3 Analytic Model of Microlens Optical Parameters

In what follows, it is useful to define the parameter η as the ratio of telescope to fiber focal-ratios

$$\eta \equiv f_{\text{tel}}/f_{\text{fib}}.$$
(1)

Appendix A then presents derivations of equations for all of the microlens design parameters (surface curvatures r_b , r_p ; thickness and spacing D_b , D_G , D_p) as a function of the telescope input

J. Astron. Telesc. Instrum. Syst.

025001-5

and fiber input focal-ratios, the size of the microimage (d_m) and the glass index n_g . As before, we equate the microimage (d_m) with the fiber core diameter.

For a fiber-microlens-based IFU, the fiber radius can be chosen based on the camera and detector size and usually ranges from 50 to 600 μ m. Thus for each d_m and $f_{\rm fib}$, we should be able to find a $f_{\rm tel}$ where the microlens radius of curvature is manufacturable while providing adequate clear aperture as well as acceptable spot size even on the edge field. At this point we can vary the telescope f-ratio and the "aperture ratio" of the beam diameter at the PC array (d) to the available aperture diameter (d_a) . All these quantities are shown in Fig. 2.

4 Model Considerations: On-Axis Aberrations

The dominant on-axis aberrations in the microlens optical system are due to sphericity and diffraction. Minimizing these as well as higher-order off-axis aberrations is desirable to maximize the EE injected into a finite fiber core. While our analytical model can deal with geometric aberrations (such as SA), the effort to minimize these depends on whether they dominate. First we show that diffraction, even for microlens systems, remains a minimal effect, which allows us to focus on the impact of minimizing SA on the lenslet design. These calculations are done at an effective wavelength of 800 nm which is the logarithmic midpoint for good fiber transmission (400 to 1600 nm), and the worse-case limit for diffraction in visible-wavelength systems.

To compare diffraction to SA we compare the impact on the radius enclosing 90% of the EE90. In case of SA, the effect can be estimated by the transverse component, i.e., the radius of circle of least confusion (CoC) which can be roughly estimated (in radians) as $d^3/(16r^3)$, where d is the diameter of the entry aperture and r is the radius of curvature. Using Eqs. (3) and (7) for d and r_p from Appendix A, we can express this as $1/(16f_{\rm fib}(n_g-1))^3$. The increase in edge field EE90 due to diffraction is simply the first minimum of the airy disk which is measured as $1.22\lambda/d$ radians. For a system which converts an f/11 telescope beam into an f/3 fiber input within a microimage diameter of $100~\mu{\rm m}$, the values of r_p and d are 0.365 and $0.267~{\rm mm}$, respectively. At 800 nm, the EE90 due to SA is more than 6 times greater than the same for diffraction. Figure 4 shows the range of $f_{\rm fib}$ and d_m (note again: we are assuming d_m is the same as the fiber core diameter) where diffraction or SA dominates for different telescope beam speed. It is interesting to note that the system tends to be more diffraction limited with slower $f_{\rm fib}$ for a given d_m and $f_{\rm tel}$. Slower $f_{\rm fib}$ would also (1) introduce additional FRD, (2) reduce the grasp of the system,

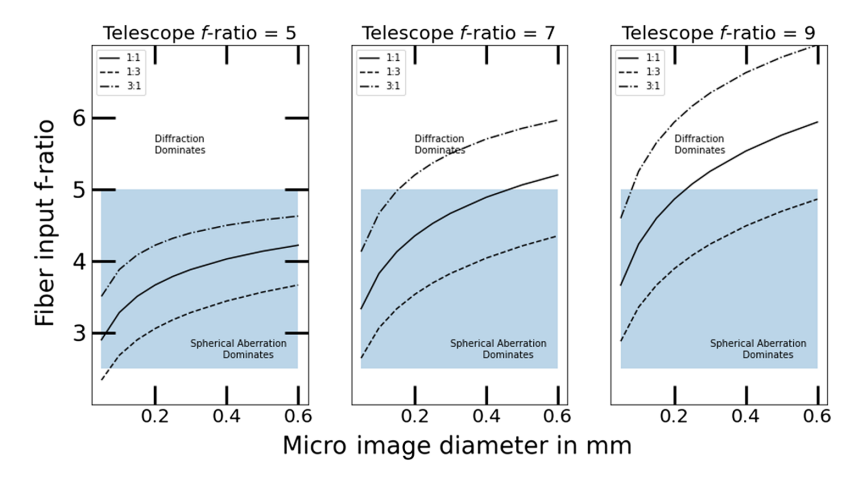


Fig. 4 Range of fiber input beam speed and microimage diameter (matched to the fiber core diameter) for which diffraction or SA dominates for different telescope beam speeds. For practical purposes, the fiber core diameter will be close to the microimage diameter. Curves indicate the ratio of the airy disk first minimum for a wavelength of 800 nm to the circle of least confusion at values of unity (solid line), 1:3 (dashed; strongly spherical-aberration limited), and 3:1 (dot-dash; strongly diffraction-limited). The aperture and radius of curvature are computed using Eqs. (3) and (7) from Appendix A. The blue-shaded region is the design target for fiber input *f*-ratio.

J. Astron. Telesc. Instrum. Syst.

025001-6

(3) reduce the radius of curvature of the optical elements; and hence are not advisable to use. Thus for practical purpose we would concentrate on the range of $f_{\rm fib}$, d_m , and $f_{\rm tel}$, where SA dominates. Our f-ratio selection range also shows that beyond $f_{\rm tel}/7$, most of our optimization space comes under systems that are mostly SA-dominated.

5 Constraining the Telescope Focal-Ratio: Minimizing Throughput Loss Due to Aberrations

Given the dominance of SA over diffraction in most applications, we use our analytic model to minimize the effect of SA on diminishing throughput. We then check if this analytic model is accurate when considering higher-order aberrations, and conclude on the limits our calculations place on the telescope focal ratio.

To minimize the effects of light loss from SA, we assume the thickness of microlens positions the CoC on the exit surface of the PC microlens (the fiber input core location). We can estimate this PC thickness as the distance from the entry into MLA to the point of crossing the optical axis by a marginal ray given the separation between the chief and the marginal ray and lenslet radius of curvature is known. This is an analytical description of the longitudinal SA. We have used this description to derive the relative constraint between PC MLA thickness and radius of curvature for a given d_a and d_m (hence η). Likewise, for a given radius of CoC (depending on how fast the PC MLA is) we can work out the losses for a fiber with a diameter of d_m . If the prescription on the PC MLA thickness and radius become too severe we can define the trade-off in photon loss outside of d_m if the CoC is not placed on the exit surface of the PC MLA.

Appendices B and C describe the analytical model to define the longitudinal and transverse SA (LSA and TSA). We found that analytical solutions to be cumbersome to define the location and radius of CoC and hence we used the numerical approach. It may be noted that the result of the analytical model is still important as an initial condition for performing optical simulation to predict precise SA losses in specific IFU design studies.

We used d/2 as the marginal ray height and normalized with r_p . Their ratio only depends on $f_{\rm fib}$ and n_g . On the other hand, the normalized paraxial focus location is $n_g/(n_g-1)$ as described in Appendix B. Given this, we compute the radius and location of CoC and marginal focus for a grid of r_2/r_p (refer to Fig. 13 in Appendix C) from 0 to 0.15 with 101 samples while the position along the optical axis had 51 samples between 3 and 3.3 mm. The result is tabulated in Table 1, which establishes the well-known facts (Ref. 47): (a) the radius of the circle of least confusion, $r_{\rm coc}$, is \sim 0.25 times the beam radius at marginal ray height; (b) the distance of CoC from paraxial

Table 1 Effect of fiber input beam speed on the location and radius of circle of least confusion. From left to right, $f_{\rm fib}$ is the fiber injection speed, pf is the paraxial focal length, mf is the focal length from the marginal ray, coc is the distance to the circle of least confusion, $r_{\rm coc}$ is the radius of the circle of least confusion, and $r_{\rm pf}$ is the beam radius at the paraxial focus. All the quantities are normalized by the PC radius of curvature. All dimensions are in mm except for ratios and f-number.

f_{fib}	pf	mf	coc	$\frac{pf - coc}{pf - mf}$	$r_{\rm coc}$	$r_{\rm pf}$	$\frac{r_{\rm coc}}{r_{\rm pf}}$
2.5	3.19	3.04	3.075	0.76	0.0056	0.0223	0.25
3	3.19	3.088	3.1125	0.76	0.003	0.0124	0.24
3.5	3.19	3.116	3.135	0.74	0.0019	0.0076	0.25
4	3.19	3.133	3.1475	0.75	0.0013	0.005	0.26
4.5	3.19	3.146	3.157	0.75	0.0009	0.0034	0.26
5	3.19	3.154	3.1625	0.76	0.0007	0.0025	0.28

focus is \sim 0.75 times the distance of marginal focus from the paraxial focus. The minor variation in TSA and LSA due to fiber input beam speed is negligible.

5.1 Accuracy of the Analytic Model

At this point, it is important to note that there is also SA as well as off-axis aberration introduced by the biconvex lens entry and exit surfaces. The analytical optimization of multisurface SA is nontrivial and hence Zemax is used for this purpose. We used optical parameters from our analytic model as initial conditions for the Zemax optimization and looked for how these parameters change after detailed optimization. This optimization accounts for higher-order aberration such as coma, astigmatism, color, etc. We used two configurations, one each in regimes where SA or diffraction dominate (refer to Fig. 4):

- 1. SA dominated regime: an f/11 telescope beam is relayed to an f/3.7 fiber input beam for a microimage diameter of 100 μ m.
- 2. Diffraction-limited regime: an f/7 telescope beam is relayed to an f/4 beam for a microimage diameter of 50 μ m.

We use Eqs. (2)–(16) for d_a and r_b from Appendix A to predict the optical parameters of the above-mentioned configurations. The analytical model is built on the assumption that the pupil should be formed at the exit surface of the BC MLA and the PC MLA is going to form the CoC at its exit surface. We then use Zemax optimization to further optimize both the configurations. Table 2 shows the comparison chart of the parameters and performance before and after

Table 2 Comparison of design parameters and performance of the reimaging microlens system based on our analytic model (Model) and after optimization using Zemax (Simulation) for different configurations in SA dominated and diffraction dominated case. The different configuration, optical, and performance parameters are (a) f_{tel} : telescope focal ratio; (b) f_{fib} : fiber input focal ratio; (c) d_m : microimage diameter at the fiber input face; (d) r_p : PC microlens radius of curvature; (e) D_p : PC microlens thickness; (f) D_G : air gap thickness between PC and BC microlens; (g) r_b : BC microlens radius of curvature; (h) D_b : BC microlens thickness; (i) d_{f0} : RMS spot size at the field center of the fiber input surface; (j) d_{f1} : RMS spot size at the field edge of the fiber input surface; (k) EE98: radius of 98% of the normalized EE at the fiber input surface. This corresponds to the reimaged patch of $d_a = d_m \times \eta$. All dimensions, except for focal ratios, are provided in μ m. Model and Simulation refer to analytical model predicted value and Zemax optimization provided value respectively.

	Dimensions are in μm	SA c	lominated	Diffraction dominated		
Configuration	(a) f _{tel}	11		7		
	(b) f_{fib}	3.7		4		
	(c) <i>d_m</i>	100		50		
		Model	Simulation	Model	Simulation	
Optical parameter	(d) r_p	333	327	68.4	114	
	(e) <i>D_p</i>	1050	994	218.4	305	
	(f) D_G	730 469		150	103	
	(g) <i>r_b</i>	999 887		126	141	
	(h) <i>D_b</i>	3160	3119	382	578	
Performance	(i) <i>d</i> _{f0}	1.207	1.121	0.317	0.4	
	(j) <i>d</i> _{f1}	3.424	2.919	3.555	1.24	
	(k) EE98	52	50	24.5	25	

J. Astron. Telesc. Instrum. Syst.

025001-8

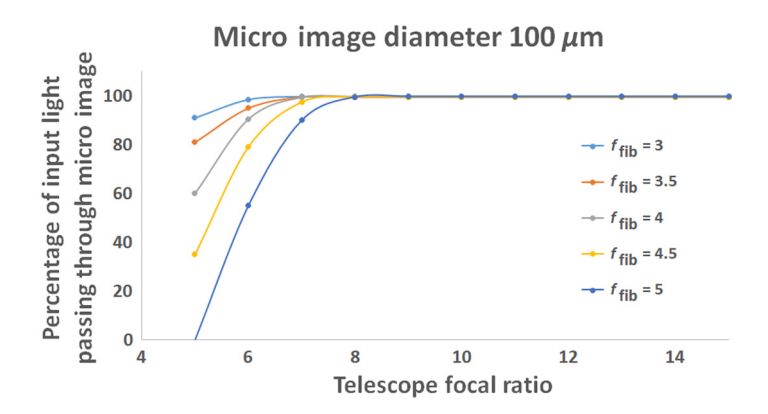


Fig. 5 Percentage of throughput captured within the microimage diameter (d_m , taken to be the same as the fiber diameter) against telescope focal-ratio for different fiber input beam speed for PC MLA assuming collimated input beam in the presence of diffraction, SA and all higher-order aberrations. Results are based on Zemax modeling. Similar results are found for microimage diameters ranging from 50 to $600\mu m$.

optimization. The design parameters change little in the SA-limited case (as we might expect), but significantly in the diffraction-limited regime. Nonetheless, we find that the analytical prediction produces optical performance similar to that of Zemax optimized design within 4% for both the SA-dominated regime and the diffraction-dominated scenario based on EE98 estimates. Since the fiber azimuthally scrambles the spatial information at its input, RMS spot radius do not provide the required estimate of performance.

5.2 Limiting Telescope Beam Speed in the Presence of Microlens Aberrations

For a single spherical lens system (e.g., just the PC MLA), intuitively one would place the CoC produced by the lens on the fiber input aperture, which is what our analytic model assumes. For a compound lens system, the situation is less obvious, however, our Zemax optimization indicates (Table 2) that placing the CoC produced by the PC MLA very close to the fiber entrance aperture remains optimal when SA dominates over diffraction on-axis.

We have used Zemax simulation to define the photon loss for a fiber capturing the CoC at its entry surface for a range of telescope and fiber input f-ratio. The throughput (provided as a percentage of input photons) captured within the microimage diameter of $100~\mu m$ for different $f_{\rm tel}$ and $f_{\rm fib}$ is plotted in Fig. 5 including the effects of diffraction and off-axis aberrations. The Figure shows that $f_{\rm tel}$ of 6, 7, 7, 8, and 8 are optimum for $f_{\rm fib}$ of 3, 3.5, 4, 4.5, and 5, respectively. Although the plot is for 100- μm microimage diameter, the optimum telescope f-ratio of f/8 or slower holds true for other microimage diameters ranging from 50 to 600 μm . This discussion can be used as a constraint on $f_{\rm tel}$ coming from aberrations and can be summarized as the following:

- 1. The faster the telescope beam, the larger the SA, as well as off-axis aberrations, hence the larger the losses.
- 2. At fast telescope beams, a fast fiber input beam helps to minimize the losses.

6 Constraining the Telescope Focal-Ratio: Microlens Manufacturing Limitations

Aberrations are not the only component that set a bound on the usable telescope focal ratio, $f_{\rm tel}$. Several optical parameters, such as the radius of curvature and thickness of PC and BC microlenses also pose constraints. In this section, we describe the limiting conditions originating from such manufacturing limitations for various microimage diameters, d_m , and fiber injection speeds, $f_{\rm fib}$. These limits are computed using our analytical model in Sec. 3. We use openly available information provided by A μ S as a benchmark for fabrication.

J. Astron. Telesc. Instrum. Syst.

025001-9

6.1 Limits on f_{tel} from Lenslet Radii of Curvature

Figures 6 and 7 show the effect of $f_{\rm fib}$, and d_m and $f_{\rm tel}$ on the required radii of curvature (RoC) for BC (r_b) and PC (r_p) MLAs, respectively. Clearly the fabrication limit on r_b does not constrain $f_{\rm tel}$ for any fiber size and injection speed consider. Similarly, for On the other hand, the fabrication limit on r_p shows that for 50- μ m fiber it is necessary for $f_{\rm tel} \ge 6$ for $f_{\rm fib} = 5$, but it does not provide any restriction for faster fiber injection speeds $f_{\rm fib} < 4$. For larger fibers $(\ge 100~\mu{\rm m})$ we can conclude broadly that there is no limiting $f_{\rm tel}$ originating from fabrication constraints on the MLA RoC.

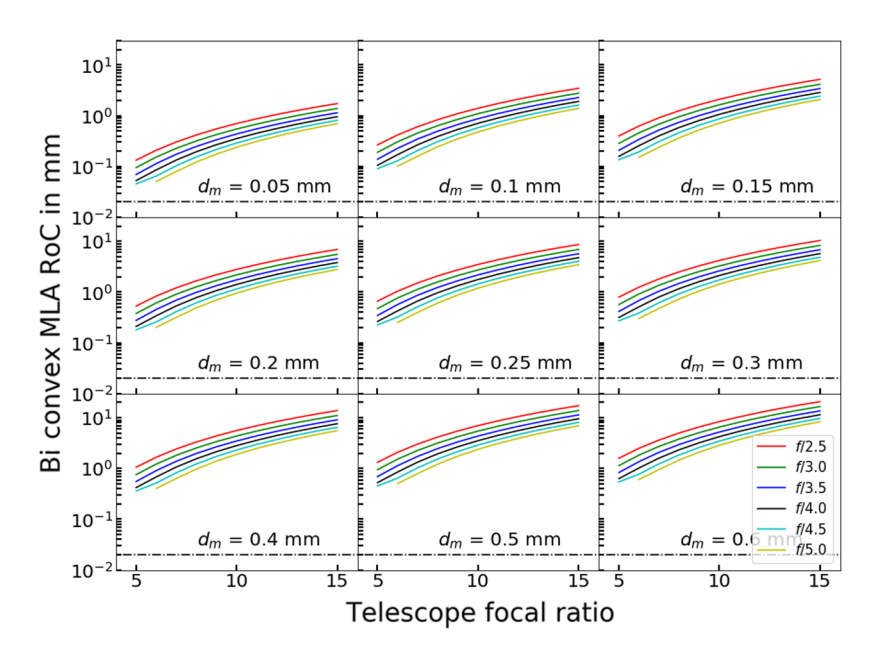


Fig. 6 Dependence of BC microlens radius of curvature (r_b) on telescope f-ratio for a range of fiber input f-ratios (different colored lines defined the bottom-right panel key) and fiber diameters, assumed here to equal to d_m . From top-left to bottom-right panels correspond to 50- to 600- μ m core fiber. Black dashed lines denote 0.02 mm, the minimum possible radius of curvature.

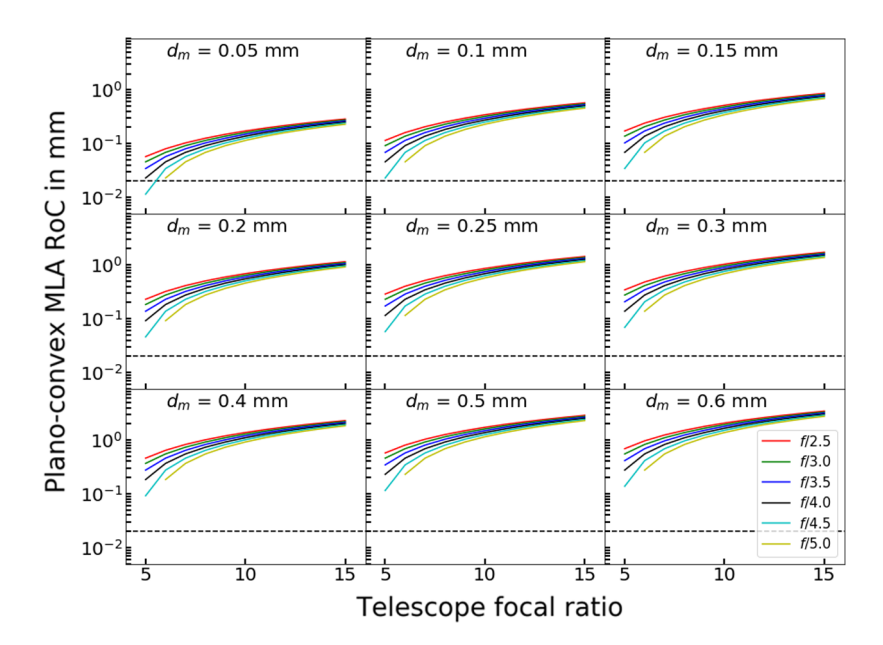


Fig. 7 Dependence of PC microlens radius of curvature (r_p) on telescope f-ratio, fiber diameter, and fiber input f-ratio as in Fig. 6. Curves are defined as in Fig. 6.

J. Astron. Telesc. Instrum. Syst.

025001-10

6.2 Limits on f_{tel} from MLA Thickness

Apart from the microlens radius of curvature, the microlens thicknesses (d_p and d_b) also constrain the telescope f-ratio range. Equations (5) and (10) in Appendix A show both d_p and d_b increase linearly with d_m and hence the manufacturable thickness could pose constraints on f_{tel} . We have computed the dependence of f_{tel} on MLA thickness for different fiber injection speeds and microimage diameters in Figs. 8 and 9.

For fabrication thickness upper limits, a PC MLA can have arbitrarily large thickness by bonding it to a flat substrate. However, for the BC MLA, the registration error between curved

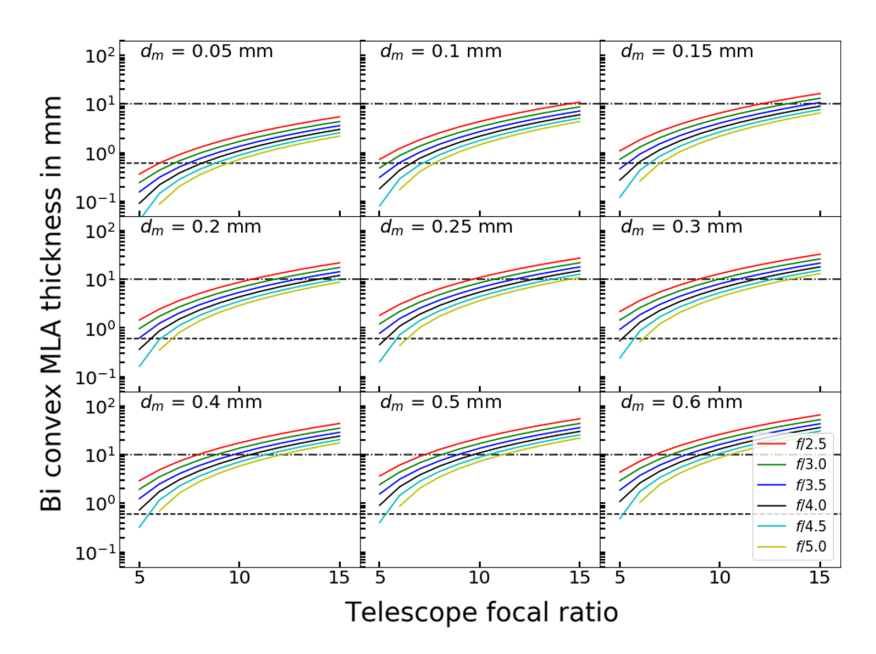


Fig. 8 Dependence of BC microlens required thickness (D_b) on telescope f-ratio, fiber diameter d_m , and fiber input f-ratio (different colored lines defined the bottom-right panel key). The dash-dot and the dashed-black lines represent the higher and the lower limit of thickness, respectively.

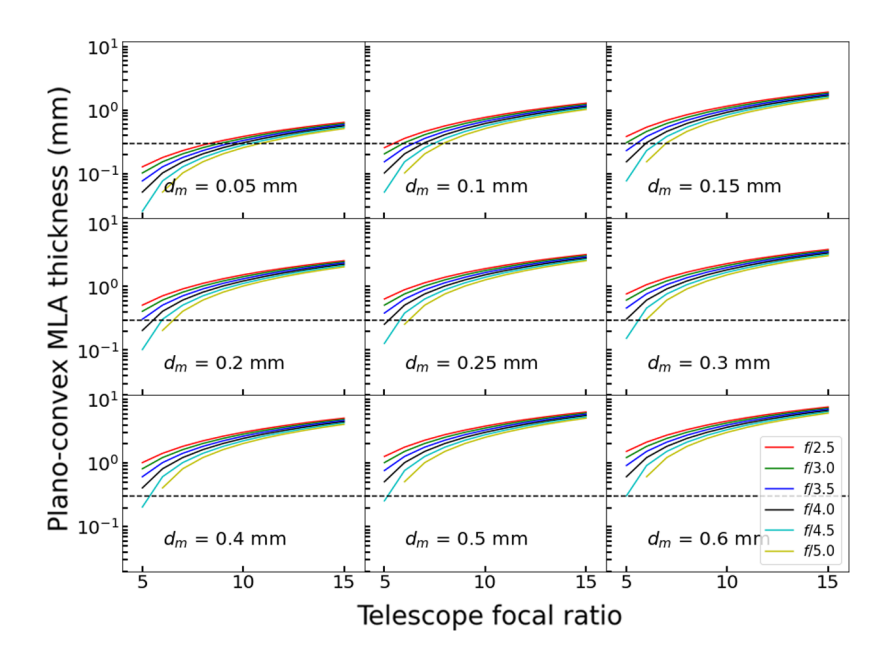


Fig. 9 Dependence of PC microlens required thickness D_p on telescope f-ratio, fiber diameter d_m , and fiber input f-ratio (different colored lines defined the bottom-right panel key). The dashed-black lines represent the thickness lower limit; the upper limit is at the upper limit of the plotting range.

J. Astron. Telesc. Instrum. Syst.

025001-11

faces increases with thickness and hence a manufacturing limit of 10 mm is used by the vendors. It should be noted that with additional effort of alignment and bonding, two PC MLAs and an arbitrarily thick glass plate can be used to eliminate the thickness upper limit. Consequently, the BC MLA thickness upper limit is taken to be a soft limit. In general, MLA thickness upper limits tend to drive the telescope speed to be faster. As can be seen in Figs. 8 and 9, a 10-mm thickness upper limit, the BC MLA sets $f_{\rm tel} \leq 7(11)$ for $f_{\rm fib} = 2.5(5)$, respectively, 600- μ m fibers. For smaller fibers with diameter $\leq 100~\mu$ m the thickness does not limit the $f_{\rm tel}$ within the range of telescope focal ratios that are being considered. The PC MLA thickness imposes no limits on $f_{\rm tel}$ as it can be increased arbitrarily.

For fabrication thickness lower limits, the manufacturer has to ensure that the array is flat and thus it is difficult to reduce lenslet thickness below 0.3 and 0.6 mm for PC and BC MLA respectively. In general, MLA thickness lower limits tend to drive the telescope speed to be slower. As can be seen in Figs. 8 and 9, the minimum thickness forces $f_{\text{tel}} \ge 9(11)$ for 50- μ m fiber for $f_{\text{fib}} = 2.5(5)$ but does not limit fibers with $\ge 400-\mu$ m cores.

6.3 Summary of Limitations on f_{tel}

Table 3 compiles all the limitations on f_{tel} from different criteria presented in this and the previous Sec. 4. In the final columns, we take the most conservative option as our final limit. In most cases, the lower limit is set by "SA," which includes the impact of all aberrations on EE98. This means that this limit is unaffected by any potential future improvements in fabrication limits for spherical lenslet figures. Aspherics may alter this picture and are worthy of future consideration. In contrast, the upper limit on f_{tel} is constrained solely by the BC MLA thickness upper limit. As described above, this upper limit may be surmountable and as such, there is no hard upper limit on the telescope beam speed.

It is evident and intuitive that faster telescope beams require the optical dimensions of the microlens arrays to be smaller and hence lossier for fiber-coupling due to increased aberrations. Less intuitive is the fact that for a larger fiber core diameter, the limiting telescope f-ratio gets faster. The effect is most pronounced going from the diffraction-limited to SA-dominated regimes (in the range 50 μ m $< d_m < 100 \ \mu$ m). Indeed, in the SA-dominated regime the limiting telescope f-ratio is constant for a given fiber input beam speed, and only changes by 33% for a factor of two changes in fiber injection speed.

We provide a visual summary of Table 3 in Fig. 10 where the final range of acceptable telescope focal ratios are plotted against fiber diameter for three fiber input beam speeds. In terms of conserving grasp, it is important to note that due to FRD it is preferable to use fiber injection speeds closer to $f_{\rm fib}=3$ than $f_{\rm fib}=5$. Overall, however, it is important to keep in mind that the grasp $(A\ \Omega)$ does not depend on the telescope focal-ratio but rather only on the square of the telescope diameter $D_{\rm tel}$ (collecting area, A), and the product of $d_m/(D_{\rm tel}\times f_{\rm fib})$ (solid angle, Ω). While the solid angle can be rewritten as $d_a/(D_{\rm tel}\times f_{\rm tel})$, fundamentally the grasp is driven by the telescope size and the considerations of the spectrograph injection speed and aperture, hence the fiber size d_m and the fiber injection speed.

As a common practice in slit spectroscopy, astronomers often need to modulate the slit width at a fixed focal ratio to optimize the resolution-throughput product of their observations given the requirements of the scientific program, the observing conditions, and the angular scale of their sources. For fiber spectroscopy, including lenslet-coupled IFUs, this is equivalent to changing the fiber core diameter at a fixed focal ratio. In this context, Fig. 10 shows that for fiber sizes $< 100 \ \mu m$ there is a limited range in fiber size that can be accommodated at a fixed telescope and fiber injection speeds. Conversely, for fiber core diameters of $100 \ \mu m$ and larger lenslet coupling can be achieved with a fixed telescope focal ratio of f/8 for fiber injection at f/3 (or f/9 to f/10 for fiber injection at f/4, etc.). Similarly, for fiber cores $> 100 \ \mu m$, there is a broader range of fiber injection speeds at a fixed telescope focal ratio in the range of 8 to 10, with f/8 providing the largest range of fiber injection speeds. On this basis, we suggest f/8 as the optimum telescope f-ratio in terms of lenslet-fiber coupling flexibility for fibers with core sizes $\geq 100 \ \mu m$. The use of smaller fibers may apply to small telescopes (below 4 m) where the science requires matching the fiber core to the seeing disk. While Fig. 10 indicates that telescope focal ratios

Table 3 Summary of limits on telescope beam speed for all configurations of varying microimage diameter at the fiber input (d_m) and fiber input beam speed (f_{fib}) . L and U denote lower and upper limits of telescope beam speed respectively while no limits are represented with dash. BC and PC represents BC and PC microlens while Abr and RoC stands for optical aberrations and radius of curvature, respectively. All constraints are from Sec. 6 except for optical aberrations (Sec. 4).

			Thick	ness			R	оС					
		В	BC		PC		SC .	PC		Abr		Final	
d _m (μm)	f_{fib}	L	U	L	U	L	U	L	U	L	U	L	U
50	2.5	6	_	9	_	_	_	_	_	6	_	9	_
	3	7	_	9	_	_	_	_	_	6	_	9	_
	3.5	8	_	10	_	_	_	_	_	7	_	10	_
	4	9	_	10	_	_	_	_	_	7	_	10	_
	4.5	9	_	11	_	_	_	6	_	8	_	11	_
	5	10	_	11	_	_	_	6	_	8	_	11	_
100	2.5	_	14	6	_	_	_	_	_	6	_	6	14
	3	6	_	7	_	_	_	_	_	6	_	7	_
	3.5	6	_	7	_	_	_	_	_	7	_	7	_
	4	7	_	7	_	_	_	_	_	7	_	7	_
	4.5	8	_	8	_	_	_	_	_	8	_	8	_
	5	8	_	8	_	_	_	_	_	8	_	8	_
200	2.5	_	10	_	_	_	_	_	_	6	_	6	10
	3	_	11	_	_	_	_	_	_	6	_	6	11
	3.5	_	12	_	_	_	_	_	_	7	_	7	12
	4	6	13	6	_	_	_	_	_	7	_	7	13
	4.5	7	14	6	_	_	_	_	_	8	_	8	14
	5	7	_	7	_	_	_	_	_	8	_	8	_
300	2.5	_	8	_	_	_	_	_	_	6	_	6	8
	3	_	9	_	_	_	_	_	_	6	_	6	9
	3.5	_	10	_	_	_	_	_	_	7	_	7	10
	4	6	11	_	_	_	_	_	_	7	_	7	11
	4.5	6	12	6	_	_	_	_	_	8	_	8	12
	5	7	13	6	_	_	_	_	_	8	_	8	13
400	2.5	_	7	_	_	_	_	_	_	6	_	6	7
	3	_	8	_	_	_	_	_	_	6	_	6	8
	3.5	_	9	_	_	_	_	_	_	7	_	7	9
	4	_	10	_	_	_	_	_	_	7	_	7	10
	4.5	6	11	6	_	_	_	_	_	8	_	8	11
	5	6	12	6	_	_	_	_	_	8	_	8	12

Table 3 (Continued).

			Thick	ness			R	оС						
		В	BC		PC		BC		PC		Abr		Final	
d _m (μm)	f_{fib}	L	U	L	U	L	U	L	U	L	U	L	U	
500	2.5	_	7	_	_	_	_	_	_	6	_	6	7	
	3	_	8	_	_	_	_	_	_	6	_	6	8	
	3.5	_	8	_	_	_	_	_	_	7	_	7	8	
	4	_	9	_	_	_	_	_	_	7	_	7	9	
	4.5	6	10	6	_	_	_	_	_	8	_	8	10	
	5	6	11	6	_	_	_	_	_	8	_	8	11	

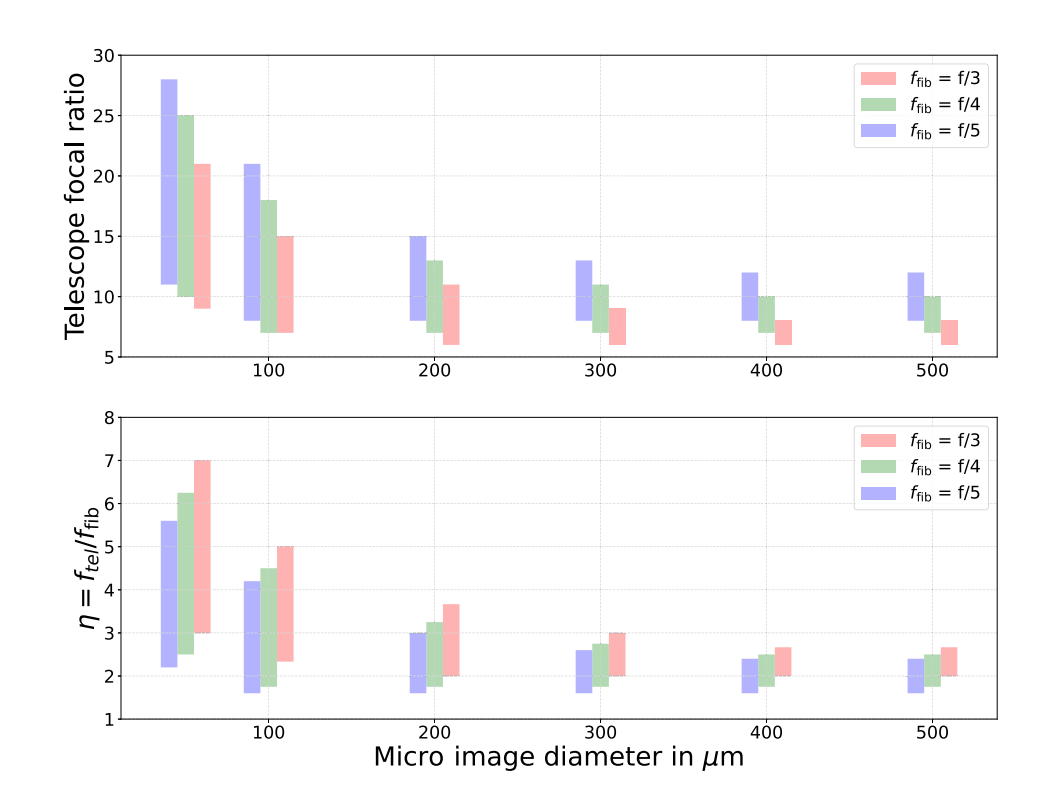


Fig. 10 Summary of Table 3 in a visual form. Range of acceptable f_{tel} is plotted against different fiber sizes for f_{fib} of f/3, f/4, and f/5.

faster than f/8 would allow for faster injection speeds for larger fibers, the faster telescope focal ratios will limit the dynamic range in fiber core size over which this is possible.

7 Summary

We presented the trade-offs in the optical design of microlens reimaging systems constrained to link telescope focal planes to fiber optics. Specifically, we have examined the constraints on telescope focal ratio for a realistic range of fiber core diameters and fiber injection speeds given (1) manufacturing limitations on microlens arrays and (2) the need to have high-efficiency coupling. For this trade study, we have developed an analytical model from first principles and two basic conditions: (a) the BC MLA should produce the pupil at its exit surface; (b) the image

J. Astron. Telesc. Instrum. Syst.

025001-14

produced by the PC MLA must be telecentric to eliminate geometric FRD. We evaluate the efficacy of the model by considering the salient performance parameter of fibers acting as photon buckets: the percentage of energy enclosed with the fiber core by the compound lenslet system. We adopt this metric rather than RMS spot radius since fibers scramble the spatial information. In this regard, the performance of the model-predicted optical design matches within 4% of optimized models using ray-trace software. We have also characterized in detail the different regimes in which these MLA systems are dominated (on-axis) by diffraction versus SA. While the detailed microlens parameters (thickness, spacing, radius of curvature) are more accurately prescribed by our analytic model in the SA limited regime, in all cases, the model designs provide better than 98% throughput apart from Fresnel losses at the glass-air boundaries in all regimes.

We computed the overall upper and lower limits on telescope focal ratio set by the fabrication limit of BC and PC MLA as well as light-losses from SA and off-axis aberrations. Lower limits on $f_{\rm tel}$ are set by considering light-losses into the fiber, while upper limits are set by the BC MLA thickness. This upper limit of $f_{\rm tel}$ may be relaxed via additional effort in replacing a monolithic BC MLA with two back-facing PC MLAs, possibly separated by a flat glass plate.

We find the telescope focal ratio lower-limit falls precipitously from the smallest fibers considered (50 μ m) to 100 μ m, which corresponds to the transition between diffraction to SA dominated regimes. For fibers >100 μ m the limiting telescope focal-ratio is given roughly by $f_{\rm tel,lower}=0.8f_{\rm fib}+4$ and $f_{\rm tel,upper}=2f_{\rm fib}+3$. For the smallest 50- μ m fibers $f_{\rm tel,lower}=1.5f_{\rm fib}+4$, with no upper limit. The case for the 100- μ m fiber core is intermediate to these two limiting cases.

For a spectrograph fed directly by fibers injected with $3 < f_{\rm fib} < 5$, we find that an f/8 telescope would support fiber diameters from 100 to 500 μ m within the optimized range. This enables a wide range of spatial and spectral resolution for survey optimization with the same telescope and spectrograph hardware. Finally, we comment that while it is always preferable to reduce the number of optical elements when possible, the native telescope focal ratio can often be reimaged by a suitable focal reducer or expander. On the basis of our analysis, we suggest such additional optics should be designed, for most applications, to deliver a focal surface feeding microlens arrays at f/8. MLA designs with additional, or aspheric surfaces may alter these conclusions, but such augmentation incurs additional cost and complexity in design, fabrication and assembly.

8 Appendix A: Derivation of Model Parameters

Here, we calculate the relationships between the critical MLA parameters (surface curvature, thickness, and spacing) as a function of the telescope input and fiber input focal-ratios and the size of the microimage, which again we take to be just slightly under-sized with respect to the fiber core diameter. The fiber input f-ratio $f_{\rm fib}$ is defined in the air while D_p and d defines the f-ratio in glass. Hence, $f_{\rm fib}$ is usually multiplied with refractive index of glass (n_g) at the system wavelength.

8.1 Optical Diameters

Relevant diameters can be computed by using the conservation of entropy (grasp) to relate the BC MLA clear aperture d_a then can be formulated as a function of microimage diameter d_m

$$d_a = \frac{f_{\text{tel}}}{\left(\frac{f_{\text{fib}}}{d_m}\right)} = d_m \eta. \tag{2}$$

From this, the beam diameter for a single field point at the input of the PC MLA (PC) is $d \le d_a - d_m$. This follows by construction in Fig. 2 due to the constraints that (1) the PC MLA diameter cannot not exceed that of the BC MLA diameter and (2) the telecentricity requirement stipulates the principal ray for the edge field-point must fall at a height of $d_m/2$ from the optical axis, while the distance between the marginal and principal ray is d/2. Hence d/2 + d/2 = d/2.

J. Astron. Telesc. Instrum. Syst.

025001-15

 $d_m/2$ has to be equal to $d_a/2$, namely the clear aperture diameter of the PC and BC lenslets. Although d can be less than $d_a - d_m$, this reduces r_p . Hence maximizing d helps minimize SA, so we take $d = d_a - d_m$. This condition for d can be rewritten with Eq. (2) as

$$d = d_m(\eta - 1). \tag{3}$$

8.2 PC MLA Thickness and Radius of Curvature

From fiber input focal ratio, one can deduce that the PC lens thickness is simply

$$f_{\rm fib}n_g = \frac{D_p}{d}. (4)$$

Note that since f-ratio is determined in air, refractive index has to be multiplied to get the f-ratio in the glass. This can be rewritten using Eq. (3) as

$$D_p = d_m n_q f_{\text{fib}}(\eta - 1). \tag{5}$$

Using the lens makers equation for plano convex lens with r_p is the radius curvature of the curved surface and the other side is flat, we can state that

$$\frac{1}{D_p/n_g} = (n_g - 1) \left(\frac{1}{r_p} - \frac{1}{\infty}\right). \tag{6}$$

Again note the use of n_g as a dividing factor as the focal length is usually defined in air but in our case the focus is the flat back plane of the MLA. Hence the thickness of PC lenslets should in air focal length multiplied by the refractive index of the glass. Hence, the PC MLA radius of curvature can then be written as

$$r_p = D_p(n_g - 1)/n_g = d_m f_{fib}(n_g - 1)(\eta - 1).$$
 (7)

8.3 MLA Spacing

Again, using the lens makers equation for plano convex lens we can find that

$$\frac{1}{D_G} = (n_g - 1) \left(\frac{1}{r_p} - \frac{1}{\infty} \right). \tag{8}$$

Since D_G is defined in air we do not need to include n_g . Hence the gap between the BC and PC MLA can be derived as

$$D_G = r_p / (n_q - 1) = d_m f_{fib}(\eta - 1). \tag{9}$$

8.4 BC MLA Thickness and Radius of Curvature

Similar to PC MLA, the BC MLA thickness can be derived as

$$D_b = n_a df_{\text{tel}} = d_m n_a f_{\text{tel}}(\eta - 1). \tag{10}$$

The BC MLA radius of curvature can be derived from the path of chief ray of the edge field inside the BC MLA as shown in Fig. 11, as follows. From Snell's law, $\sin \theta = n_g \sin \beta$, and from Fig. 11 we have $\theta = \alpha + \beta$.

From this, we can easily derive

$$\tan \beta = \frac{\sin \alpha}{n_q - \cos \alpha},\tag{11}$$

J. Astron. Telesc. Instrum. Syst.

025001-16

Chattopadhyay et al.: Optimum telescope focal ratios for microlens-to-fiber coupled integral...

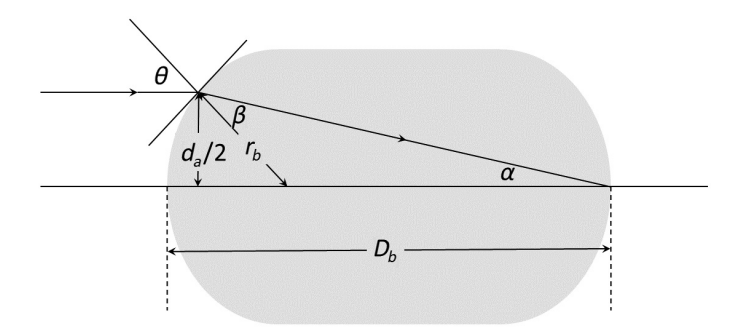


Fig. 11 Propagation path of edge field chief ray inside the BC lenslet.

while from the right angle triangle we can define $\sin \alpha$ as

$$\sin \alpha \approx \frac{d_a/2}{\sqrt{(d_a/2)^2 + D_b^2}},\tag{12}$$

and similarly

$$\sin(\alpha + \beta) = \frac{d_a/2}{r_b},\tag{13}$$

which we can combine to write

$$\tan \beta = \frac{d_a/2}{\sqrt{(n_g r_b)^2 - (d_a/2)^2}}.$$
 (14)

From Eqs. (11) and (14), we can easily define the radius of the BC MLA as

$$r_b = \frac{1}{n_g} [(n_g \sqrt{(d_a/2)^2 + D_b^2 - D_b})^2 + (d_a/2)^2]^{1/2},$$
(15)

for which Eqs. (2) and (10) can be used to express r_b in terms of f_{tel} , f_{fib} (or f_{tel} and η), and d_m

$$r_b = d_m \eta \left[\left(\sqrt{1/4 + (n_q f_{\text{fib}}(\eta - 1))^2} - f_{\text{fib}}(\eta - 1) \right)^2 + 1/(4n_q^2) \right]^{1/2}.$$
 (16)

9 Appendix B: Refraction on the Spherical Surface: Dependence of Microlens Thickness on Beam Diameter

Here, we define the PC MLA thickness, f (sag plus flat thickness), with radius of curvature R, such that the ray of an object at infinity at height r crosses the optical axis at the exit surface. Due to SA, this thickness depends on height. We have defined the thickness for an object at infinity and in line with our requirement of treating the PC MLA which is the imaging lens in our system. This generic description of MLA thickness will help us define the PC lenslet parameters required to locate the CoC on the PC MLA exit surface in the next subsection. Using the derivation from Hecht⁴⁸ for an object at a distance S_o in front of the MLA, illustrated in Fig. 12, their Eq. (5.4), given here as

$$\frac{n_1(S_o + R)}{l_o} = \frac{n_2(S_i - R)}{l_i},\tag{17}$$

can be rewritten for an object at infinity $(S_o = l_o = \infty, S_i = f, n_1 = 1 \text{ and } n_2 = n_q)$

$$n_a(f - R) = l_i. (18)$$

J. Astron. Telesc. Instrum. Syst.

025001-17

Chattopadhyay et al.: Optimum telescope focal ratios for microlens-to-fiber coupled integral...

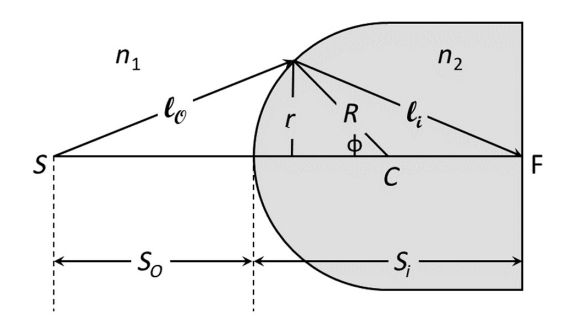


Fig. 12 Derivation of PC microlens focal length.

It is straightforward to construct

$$l_i = [R^2 + (f - R)^2 + 2R(f - R)^2 \cos \phi]^{1/2}, \tag{19}$$

where $\cos \phi = \sqrt{1 - (\frac{r}{R})^2}$. Solving for f - R we arrive at an expression for f

$$f = R \left[1 + \frac{1}{\sqrt{n_g^2 - (\frac{r}{R})^2} - \sqrt{1 - (\frac{r}{R})^2}} \right],\tag{20}$$

which has the expected paraxial approximation $(r/R \ll 1)$ of $f = R(n_g/(n_g - 1))$. The dependence of the microlens thickness f on (r, R, n_g) is simply the manifestation of SA on a collimated beam.

10 Appendix C: Effect of Spherical Aberration on Microlens Focal Length: Longitudinal and Transverse Spherical Aberration

The longitudinal SA (LSA) is defined by the distance between paraxial focus and the focus of the marginal ray while the transverse SA (TSA) is the marginal ray height at the paraxial focus. However, to minimize the effect of SA the location and radius of CoC are important to understand. The location would directly define the thickness of the PC lenslet while the CoC radius would impose condition on the lenslet properties to restrict the microimage to form within the fiber core to reduce photon loss at the MLA-fiber junction. Increasing the fiber core diameter arbitrarily to engulf entire microimage would lead to an increase in optical entropy which can be equated to loss of observation time.

Now having the analytical description of the thickness of PC lenslet in our arsenal, we will describe the radius and position of circle of least confusion and what should be the strategy for minimizing the radius. In Fig. 13, we define a PC microlens of radius of curvature R fed with a collimated beam. The height of the ray from the optical axis is r; α and β are the angles of incidence and refraction at the input surface, respectively; q and δ are the distances of the crossing of optical axis inside the microlens and chief ray entry point to the arbitrary ray entry point respectively. Suffixes 1 and 2 denote angles and dimensions associated with marginal and paraxial ray, respectively. The radius of the CoC is defined as r_3 while the distance from circle of least confusion from the marginal ray focus is γ .

It is easy to find that $\delta_2 = R - \sqrt{R^2 - r_2^2}$. We can also deduce the following:

$$\frac{r_3}{\gamma} = \frac{r_1}{\sqrt{R^2 - r_1^2}},\tag{21}$$

and

J. Astron. Telesc. Instrum. Syst.

025001-18

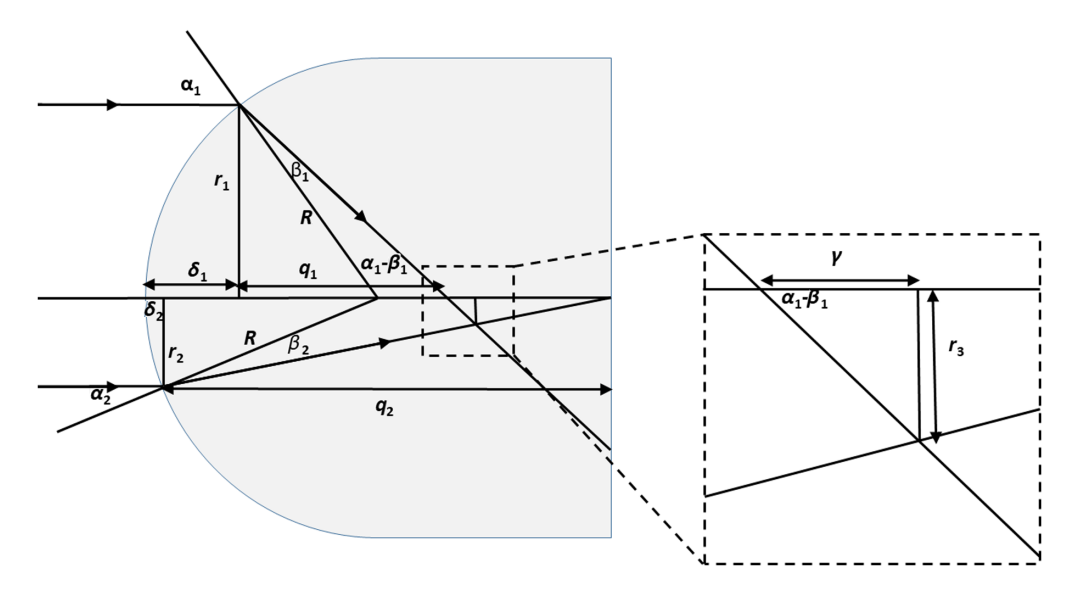


Fig. 13 Derivation of position and radius of circle of least confusion.

$$\frac{r_2}{r_3} = \frac{f(r_2) - \delta_2}{f(r_2) - f(r_1) - \gamma}.$$
 (22)

Solving Eqs. (17) and (18) we get

$$r_3 = \frac{r_1 r_2 (f(r_2) - f(r_1))}{r_1 [f(r_2) - R + \sqrt{R^2 - r_2^2}] + r_2 \sqrt{R^2 - r_1^2}},$$
(23)

and

$$\gamma = \frac{r_2\sqrt{R^2 - r_1^2}(f(r_2) - f(r_1))}{r_1f(r_2) - r_1(R - \sqrt{R^2 - r_2^2}) + r_2(R - \sqrt{R^2 - r_1^2})}.$$
 (24)

One can differentiate Eq. (23) and find the maxima to identify the location of the CoC. However, this analytical approach is quite cumbersome and hence it is better to solve the problem numerically.

References

- 1. G. J. Hill et al., "Design, construction, and performance of VIRUS-P: the prototype of a highly replicated integral-field spectrograph for HET," *Proc. SPIE* **7014**, 701470 (2008).
- 2. M. H. Fabricius et al., "VIRUS-W: an integral field unit spectrograph dedicated to the study of spiral galaxy bulges," *Proc. SPIE* **7014**, 701473 (2008).
- 3. H. Sugai et al., "Prime Focus Spectrograph for the Subaru telescope: massively multiplexed optical and near-infrared fiber spectrograph," *J. Astron. Telesc. Instrum. Syst.* **1**(3), 035001 (2015).
- 4. A. Hill et al., "Maunakea spectroscopic explorer (MSE): instrumentation suite," *Proc. SPIE* **10702**, 107021L (2018).
- 5. B. Flaugher, "The dark energy survey," *Int. J. Mod. Phys. A* 20, 3121–3123 (2005).
- 6. R. de Jong et al., "4most: 4-metre multi-object spectroscopic telescope," *Proc. SPIE* **9147**, 91470M (2014).
- 7. N. P. Konidaris et al., "SDSS-V local volume mapper instrument: overview and status," *Proc. SPIE* **11447**, 1144718 (2020).
- 8. M. A. Bershady et al., "SparsePak: a formatted fiber field unit for the WIYN telescope bench spectrograph. I. Design, construction, and calibration," *Publ. Astron. Soc. Pac.* **116**, 565–590 (2004).

J. Astron. Telesc. Instrum. Syst.

025001-19

- 9. M. M. Roth et al., "PMAS: the potsdam multi-aperture spectrophotometer. I. design, manufacture, and performance," *Publ. Astron. Soc. Pac.* **117**(832), 620–642 (2005).
- 10. N. Drory et al., "The MaNGA integral field unit fiber feed system for the Sloan 2.5 m telescope," *Astron. J.* **149**, 77 (2015).
- 11. A. G. de Paz et al., "MEGARA, the new intermediate-resolution optical IFU and MOS for GTC: getting ready for the telescope," *Proc. SPIE* **9908**, 99081K (2016).
- 12. S. M. Croom et al., "The Sydney-AAO multi-object integral field spectrograph," *Mon. Not. R. Astron. Soc.* **421**, 872–893 (2012).
- 13. K. Bundy et al., "Overview of the SDSS-IV MaNGA survey: mapping nearby galaxies at apache point observatory," *Astrophys. J.* **798**, 7 (2015).
- 14. E. Giro et al., "BIGRE: a new double microlens array for the integral field spectrograph of SPHERE," *Proc. SPIE* **7014**, 70143K (2008).
- 15. R. Bacon et al., "The MUSE second-generation VLT instrument," *Proc. SPIE* **7735**, 773508 (2010).
- 16. R. Sharples et al., "KMOS: a multi-object deployable-IFU spectrometer for the ESO VLT," *New Astron. Rev.* **50**(4), 370–373 (2006).
- 17. P. Morrissey et al., "The Keck cosmic web imager: a capable new integral field spectrograph for the W. M. Keck observatory," *Proc. SPIE* **8446**, 844613 (2012).
- A. D. Eigenbrot, M. A. Bershady, and C. M. Wood, "The impact of surface-polish on the angular and wavelength dependence of fiber focal ratio degradation," *Proc. SPIE* 8446, 84465W (2012).
- 19. J. Allington-Smith et al., "End effects in optical fibres," *Mon. Not. R. Astron. Soc.* 436, 3492–3499 (2013).
- 20. E. Carrasco and I. R. Parry, "A method for determining the focal ratio degradation of optical fibres for astronomy," *Mon. Not. R. Astron. Soc.* **271**, 1–12 (1994).
- I. R. Parry, "Optical fibres for integral field spectroscopy," New Astron. Rev. 50(4), 301–304 (2006).
- L. W. Ramsey, "Focal ratio degradation in optical fibers of astronomical interest," in *Fiber Optics in Astronomy*,S. C. Barden, Ed., Astronomical Society of the Pacific Conference Series, Vol. 3, pp. 26–39 (1988).
- 23. J. D. Murphy et al., "Focal ratio degradation and transmission in VIRUS-P optical fibers," *Proc. SPIE* **7018**, 70182T (2008).
- 24. J. J. Bryant et al., "Focal ratio degradation in lightly fused hexabundles," *Mon. Not. R. Astron. Soc.* 438, 869–877 (2014).
- S. Chattopadhyay et al., "Optimization of telescope focal ratios for MLA-fiber coupled integral field units," *Proc. SPIE* 11451, 1145168 (2020).
- S. Chattopadhyay et al., "Fiber positioning in microlens-fiber coupled integral field unit," J. Astron. Telesc. Instrum. Syst. 6(2), 025002 (2020).
- H. Lee et al., "VIRUS-2 for the Harlan J. Smith telescope of the McDonald Observatory," *Proc. SPIE* 10702, 107028E (2018).
- 28. H. Lee et al., "Mix and match as you go: beam switch module that splits wavelengths, scrambles beams, and switches fibers in multiplexed replicated astronomical spectrograph systems such as VIRUS2," *Proc. SPIE* **11451**, 1145126 (2020).
- 29. G. J. Hill et al., "VIRUS2: a next generation replicated integral field spectrograph with wide field and broad wavelength coverage," *Proc. SPIE* **11447**, 1144716 (2020).
- 30. T. S. Chonis et al., "Design and construction progress of LRS2-B: a new low resolution integral-field spectrograph for the Hobby-Eberly Telescope," *Proc. SPIE* **8446**, 84462T (2012).
- 31. H. Lee et al., "LRS2: a new low-resolution spectrograph for the Hobby-Eberly Telescope," *Proc. SPIE* **7735**, 77357H (2010).
- 32. D. Lee et al., "Characterization of lenslet arrays for astronomical spectroscopy," *Publ. Astron. Soc. Pac.* **113**, 1406–1419 (2001).
- 33. C. G. Wynne, "Telecentricity in fibre-fed spectrographs," *Mon. Not. R. Astron. Soc.* **260**, 307–316 (1993).
- 34. F. C. Gillett et al., "The Gemini telescopes project (invited paper)," in *Revista Mexicana de Astronomia y Astrofisica Conference Series*, E. Falco, J. A. Fernandez, and R. F. Ferrero, Eds., Vol. 4, p. 75 (1996).

- 35. J. E. Gunn et al., "The 2.5 m telescope of the Sloan digital sky survey," *Astronomical Journal* **131**, 2332–2359 (2006).
- 36. J. Allington-Smith et al., "Integral field spectroscopy with the Gemini multiobject spectrograph. I. Design, construction, and testing," *Publ. Astron. Soc. Pac.* **114**, 892–912 (2002).
- 37. https://www.amus.de
- 38. A. Eigenbrot and M. A. Bershady, "Vertical population gradients in NGC 891. I. ∇Pak instrumentation and spectral data," *Astrophys. J.* **853**, 114 (2018).
- A. H. Szentgyorgyi et al., "Hectochelle: a multiobject echelle spectrograph for the converted MMT," *Proc. SPIE* 3355, 242–252 (1998).
- 40. H. Flores et al., "Giraffe multiple integral field units at VLT: a unique tool to recover velocity fields of distant galaxies," *Astron. Astrophys.* **420**(3), L31–L34 (2004).
- 41. M. Bershady et al., "WIYN bench upgrade: a revitalized spectrograph," *Proc. SPIE* **7014**, 70140H (2008).
- 42. S. A. Smee et al., "The multi-object, fiber-fed spectrographs for the Sloan digital sky survey and the Baryon oscillation spectroscopic survey," *Astron. J.* **146**, 32 (2013).
- M. Mateo et al., "M2FS: the Michigan/Magellan fiber system," Proc. SPIE 8446, 84464Y (2012).
- 44. G. Dalton et al., "WEAVE: the next generation wide-field spectroscopy facility for the William Herschel Telescope," *Proc. SPIE* **8446**, 84460P (2012).
- 45. H. Chung et al., "Dotifs: a new multi-IFU optical spectrograph for the 3.6-m Devasthal optical telescope," *Proc. SPIE* **9147**, 91470V (2014).
- R. Yan et al., "The prototype telescope and spectrograph system for the AMASE project," *Proc. SPIE* 11447, 114478Y (2020).
- 47. D. J. Schroeder, Astronomical Optics, Academic Press, San Diego (1987).
- 48. E. Hecht, *Optics*, Pearson Education Limited, England (2012).

Sabyasachi Chattopadhyay is currently a postdoctoral research fellow at the South African Astronomical Observatory working on the Slit Mask Integral Field Unit for the South African Large Telescope. He has worked at University of Wisconsin-Madison after receiving his PhD in astronomy from the Inter University Center for Astronomy & Astrophysics, Pune for developing Devasthal Optical Telescope Integral Field Spectrograph. His field of interest is fiber spectroscopic instrumentation and evolution of galaxies.

Matthew A. Bershady is a professor in the Department of Astronomy and Ciriacks Faculty Fellow in the College of Letters & Science at the University of Wisconsin-Madison, where he currently serves as project scientist for the Sloan Digital Sky Survey-IV. He is also a South African Research chair at the South African Astronomical Observatory and in the Department of Astronomy at the University of Cape Town.

Marsha J. Wolf is a senior scientist at the University of Wisconsin-Madison. She received her BS degree in electrical engineering from Kettering University (1986), her MS degree in electro-optics from the University of Dayton (1991), and her PhD in astronomy from the University of Texas at Austin (2005). Her research interests include astronomical instrumentation and the coevolution of galaxies and their AGN. She is a member of SPIE.

Michael P. Smith is a mechanical engineer who has been working on astronomy projects for 18 years at both the University of Wisconsin and University of Texas. He has played major roles in the development of instruments for the Southern African Large Telescope, Hobby Eberly Telescope, the WIYN Telescope and the Sloan Digital Sky Survey. Projects have included the development of spectrographs (visible and near infrared), detector systems, fiber integral field units, and telescope subsystems.